

**Effect of microstructural anisotropy on fracture toughness of hot rolled
13Cr ODS steel – the role of primary and secondary cracking**

Das, A.; Viehrig, H. W.; Bergner, F.; Heintze, C.; Altstadt, E.; Hoffmann, J.;

Originally published:

May 2017

Journal of Nuclear Materials 491(2017), 83-93

DOI: <https://doi.org/10.1016/j.jnucmat.2017.04.059>

Perma-Link to Publication Repository of HZDR:

<https://www.hzdr.de/publications/Publ-25455>

Release of the secondary publication
on the basis of the German Copyright Law § 38 Section 4.

CC BY-NC-ND

Effect of microstructural anisotropy on fracture toughness of hot rolled 13Cr ODS steel – the role of primary and secondary cracking

A. Das^{1,a}, H.W. Viehrig^a, F. Bergner^a, C. Heintze^a, E. Altstadt^a, J. Hoffmann^b

^a Helmholtz-Zentrum Dresden-Rossendorf, Bautzner Landstrasse 400, 01328 Dresden (Germany)

^b Institute for Applied Materials, Karlsruhe Institute of Technology, Hermann-von-Helmholtz-Platz 1, 76344 Eggenstein-Leopoldshafen, Germany

¹⁾ Corresponding author, e-mail: a.das@hzdr.de

Abstract

ODS steels have been known to exhibit anisotropic fracture behaviour and form secondary cracks. In this work, the factors responsible for the anisotropic fracture behaviour have been investigated using scanning electron microscopy and electron backscatter microscopy. Fracture toughness of hot rolled 13Cr ODS steel was determined using unloading compliance method for L-T and T-L orientations at various temperatures. L-T orientation had higher fracture toughness than T-L orientation and also contained more pronounced secondary cracking. Secondary cracks appeared at lower loads than primary cracks in both orientations. Primary crack propagation was found to be preferentially through fine grains in a bimodal microstructure. Grains were aligned and elongated the most towards rolling direction followed by T and S directions resulting in fracture anisotropy. Crystallographic texture and preferential alignment of Ti enriched particles parallel to rolling direction also contributed towards fracture anisotropy.

Keywords

ODS-steel, fracture behaviour, anisotropy, secondary cracking, bimodal microstructure, delamination, fractography

Highlights

- Primary crack propagation was preferentially through fine grains
- Crack propagation was easier along rolling direction due aligned and elongated grains
- Secondary cracks initiated at lower loads than primary cracks
- Secondary cracks retarded and stabilized primary crack growth
- Fracture anisotropy depends on crystallographic texture and alignment of Ti enriched particles along rolling direction

1 Introduction

Oxide dispersion strengthened (ODS) steels are candidate materials for fuel cladding tubes in Gen-IV nuclear fission reactors [1] which are manufactured using cold pilgering process. Despite having good high temperature strength [2,3] and irradiation swelling resistance [4], ODS steels suffer from considerably higher ductile to brittle transition temperatures (DBTT) and poor fracture toughness values as compared to ferritic martensitic (F/M) steels [5].

Anisotropic fracture behaviour, both in terms of primary and secondary cracking has been observed for various hot rolled and hot extruded ODS steels [5–14]. The explanation for this anisotropic fracture behaviour has been a point of debate. Byun et al. [9] reported debonding of oxide coated aggregates of grains formed in the canning process after milling while others [11,15–17] have mentioned segregation of carbides and oxides at grain boundaries promoting inter-granular fracture along elongated grains.

Secondary cracks propagate in a plane perpendicular to the primary crack plane and are formed due to a triaxial stress state. Secondary cracks, also sometimes described as splitting [6–8,18] or delamination [8,11,18,19], are a striking feature often observed on fracture surfaces of tensile [7,9,10,20,21], Charpy impact [6,8,11–13] and fracture toughness compact tension (C(T)) specimen [5,14] from ODS materials tested close to room temperature (RT). This phenomenon has also occasionally been observed in some non-ODS steels, e.g. low carbon steels [18,19] and F/M steels [22,23], however, it appears to be less common.

Beneficial cracking behaviour which enhances the fracture toughness can be obtained if the exact knowledge of the influence of primary and secondary crack on fracture toughness with respect to anisotropic microstructure is known. In this work, we have studied the effect of anisotropic microstructure on primary and secondary crack propagation in a hot rolled 13Cr ODS steel. Hot rolling is a commonly used post processing technique for manufacturing thin plates which produces similar anisotropic elongated microstructural features as cold pilgering. Fracture toughness tests using small scale C(T) specimen were performed in the temperature range from -100°C to 700°C in L-T and T-L orientations. It was sufficient to select these two orientations in order to exploit the microstructural anisotropy of the hot rolled plate. Electron back scatter diffraction (EBSD) was used to investigate primary crack propagation in both orientations. Scanning electron microscopy (SEM) was performed on primary crack fracture surfaces to reveal more information about the mode of fracture. Secondary cracks in terms of their frequency of occurrence and depths in L-T and T-L oriented samples were compared. Finally, an explanation for anisotropic fracture behaviour was proposed.

2 Materials and methods

2.1 Material

A 13%Cr ODS steel hot rolled plate was provided by Karlsruhe Institute of Technology, Germany (KIT). The chemical composition of the material is given in Table 1. The main production steps were: mechanical alloying in an attritor ball mill, encapsulation of the powder, evacuation of the capsule and hot isostatic pressing at 1100°C and 100 MPa and rolling at 1100°C from a diameter of 80 mm to a plate of 8 mm thickness in 5 runs. Details of the production can be found in [24].

Table 1: Chemical composition of the investigated ODS alloy (wt.%)

Cr	W	Ti	Y ₂ O ₃	C	Ni	N
13.1	1.11	0.151	0.3	0.21	0.09	0.01

2.2 Fracture mechanics specimens

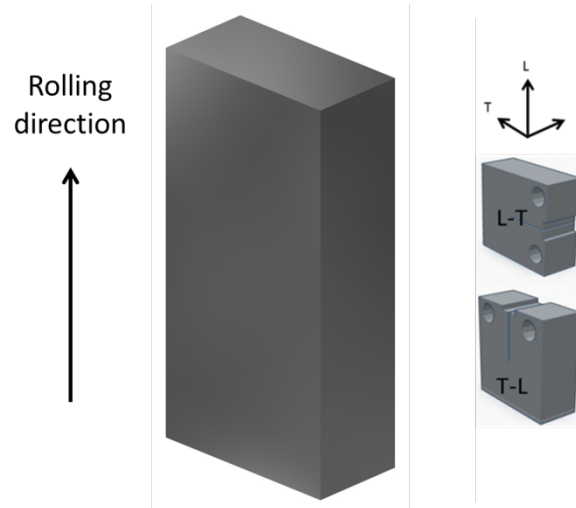


Fig. 1 Cutting scheme for L-T and T-L oriented specimen

Miniature compact tension C(T) specimen of 6.35 mm (0.25T) thickness were machined from the 8 mm plate in two orientations, L-T and T-L. The cutting scheme of the specimens can be seen in Fig. 1. All the C(T) specimens were 20% side grooved and fatigue pre-cracked at room temperature to a crack length to width ratio (a/W) of 0.5 using a resonance testing machine. The nominal cyclic stress intensity at the end of fatigue pre-cracking stage (K_{end}) was 14 MPa \sqrt{m} .

2.3 Quasi-static fracture toughness testing

Quasi-static fracture toughness tests were carried out on small size C(T) specimens in L-T and T-L orientation using the unloading compliance method [25]. The unloadings were done with 25% load drop and 30 s relaxation time. Single tests were done at -100, 22, 100, 200, 400, 500, 600 and 700 °C in air. The crosshead speed of the machine was 0.1 mm per minute with displacement steps of 0.015 mm. The tests were stopped after about 1 mm crack propagation and thereafter the specimens were heat tinted. The initial and the final primary crack lengths were measured at the fracture surfaces using optical microscope according to the nine point standard ASTM method [26]. The crack opening displacement (COD) measurements were done on the front face using a contact clip on gauge from Sandner (EXRC3-1o) in the temperature range from -100 °C to 200 °C and using a contactless video extensometer (model NG, Messphysik version 6.6.0.0) from 200 °C to 700 °C. As the 0.25T specimens had front face geometry, the compliance and displacement values had to be post converted to load line values [27]. Thereafter the evaluation was performed using ASTM E1820-13 [26]. Interrupted fracture toughness test were performed on a T-L oriented specimen and loaded in the elastic range.

2.4 Tensile tests

Tensile tests were performed at Karlsruhe Institute of Technology, Germany. Miniature cylindrical tensile test specimens, with gauge length parallel to rolling direction, were tested at

temperatures varying from 20 °C to 700 °C. The gauge length and diameter were 7 mm and 2 mm, respectively. The tests were performed in air with a test velocity of 0.1 mm/min.

2.5 Microscopy

Basic characterization

Bulk samples were polished using polycrystalline diamond solution down to 1 µm and then etched (50ml distilled water, 15 ml hydrochloric acid, 2.5 g Iron (III) chloride). Scanning electron microscopy (SEM) was performed (Zeiss EVO 50) on etched bulk samples using an accelerating voltage of 15 kV, 2.6 A filament current, probe current of 200 pA and working distance of 11 mm at various magnifications ranging from 50X to 10000X. Energy dispersive X-ray spectroscopy (EDS) was performed on etched samples using a higher spot size (probe current: 1000 pA) with a working distance of 18 mm to identify precipitates and inclusions. Back scattered mode in SEM was used on OP-S polished samples (10-30% amorphous silica, 50-70% water, 5-20% 1,3 butanediol) to obtain grain contrast and information about particle alignment. Electron back scatter diffraction (EBSD) was performed on OP-S polished samples using Zeiss NVision 40 SEM to obtain information about crystallographic texture and grain distribution. A step size varying from 48 nm to 0.19 µm was used with a pixel resolution of 800 X 600 (20 kV accelerating voltage and 18 mm working distance). The exposure time varied from 7 to 12 ms. A misorientation angle of 10° was chosen to identify high angle grain boundaries during grain distribution analysis. Bright field TEM images were taken at KIT. Particle size analysis was done using thresholding on approximately 2000 particles to calculate the feret diameters of nano-particles.

Fracture behaviour

EBSD was used to investigate primary crack propagation. After the fracture mechanics tests, the side surfaces of C(T) specimens which included the propagated primary cracks, were OP-S polished and investigated using EBSD. Stereoscopic microscope imaging (Nikon SMZ-U) was done on all fractured surfaces for macroscopic images. SEM was performed on all fracture surfaces for higher magnification images. Optical microscopy (Leica REICHERT MEF4) was done on polished planes perpendicular to secondary crack planes to measure secondary crack depths.

3 Results

3.1 Basic characterization of the microstructure

The average oxide particle size was found to be 3.8 nm by TEM analysis (Fig. 2). Ti enriched particles aligned parallel to the rolling direction were found using EDS on an etched sample (Fig. 3a). Some pre-existing cracks were also observed elongated towards the rolling direction. The backscattered image in Fig. 3b confirms the alignment of Ti enriched particles along rolling direction. OP-S polishing resulted in fall out of the particles leaving behind voids of the same size.

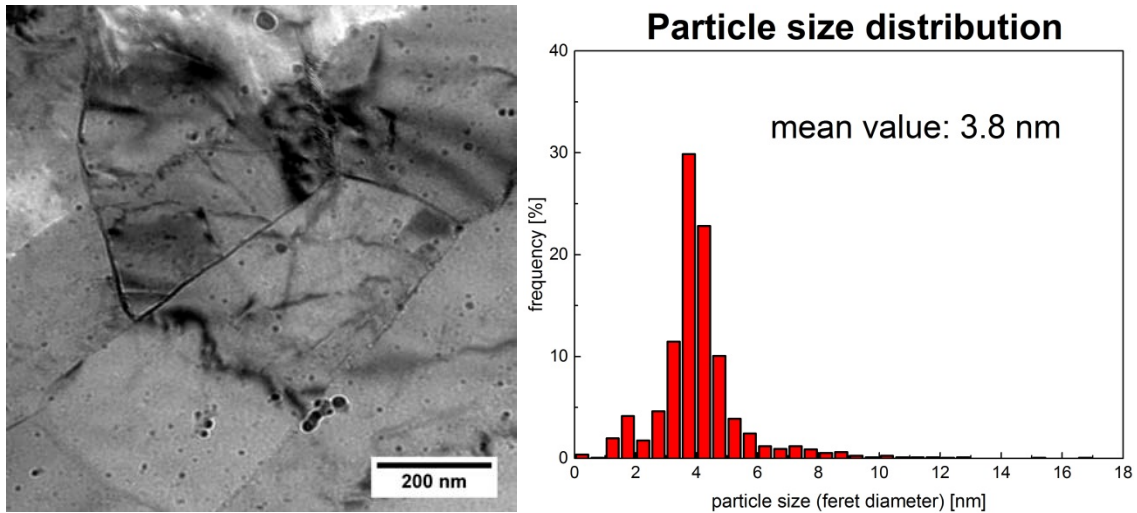


Fig. 2 TEM image and particle size distribution of hot rolled 13Cr ODS Steel

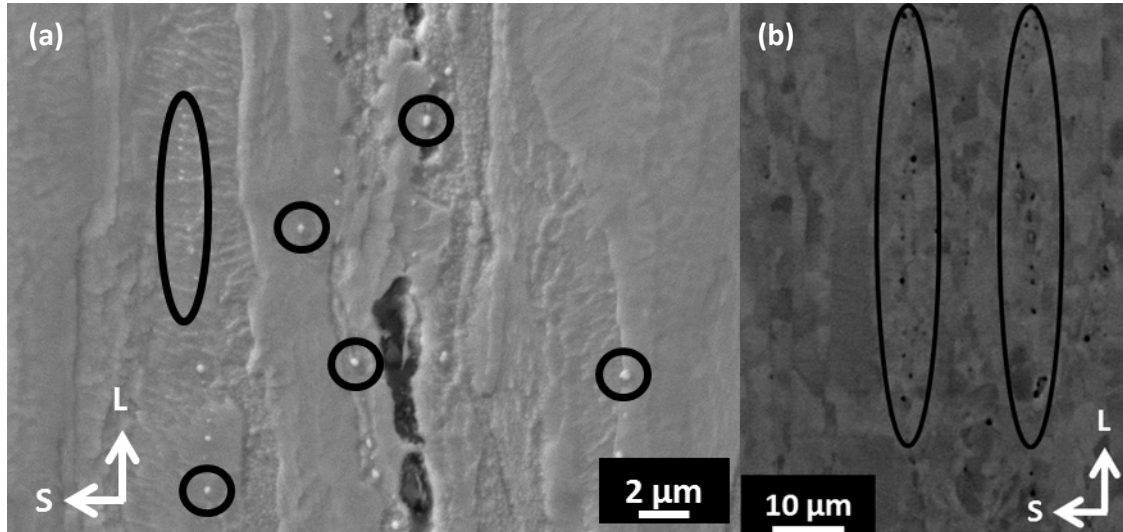


Fig. 3 SEM images showing Ti enriched aligned particles (encircled) found by EDS on etched surface along with some pre-existing cracks (a) and Back scattered image of OP-S polished surface showing aligned holes formed after Ti enriched particle fall out (b)

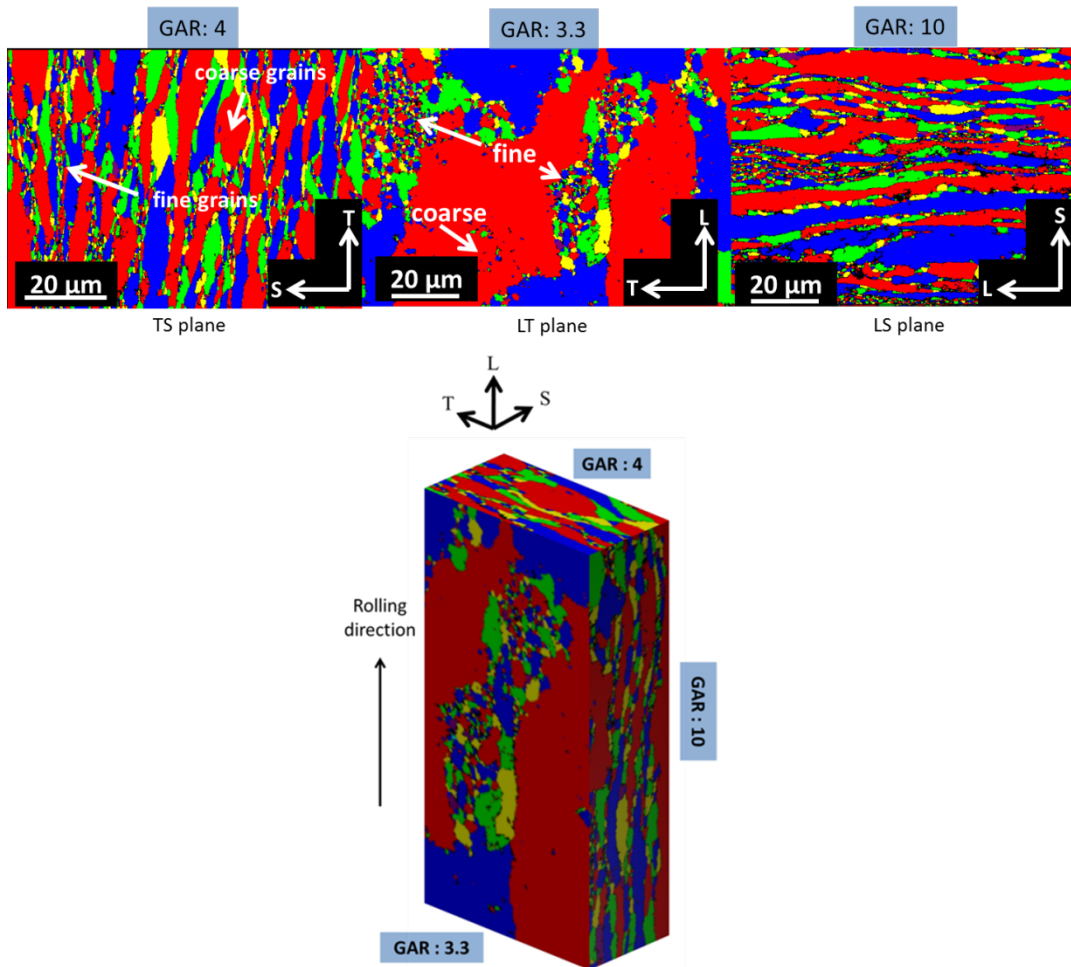


Fig. 4 Grain distribution map of TS, LT and LS planes (10° maximum misorientation angle). A schematic representation (below) of the hot rolled material with 'pancake shaped' elongated grains (not to scale). Indicated GAR values are for coarse grains

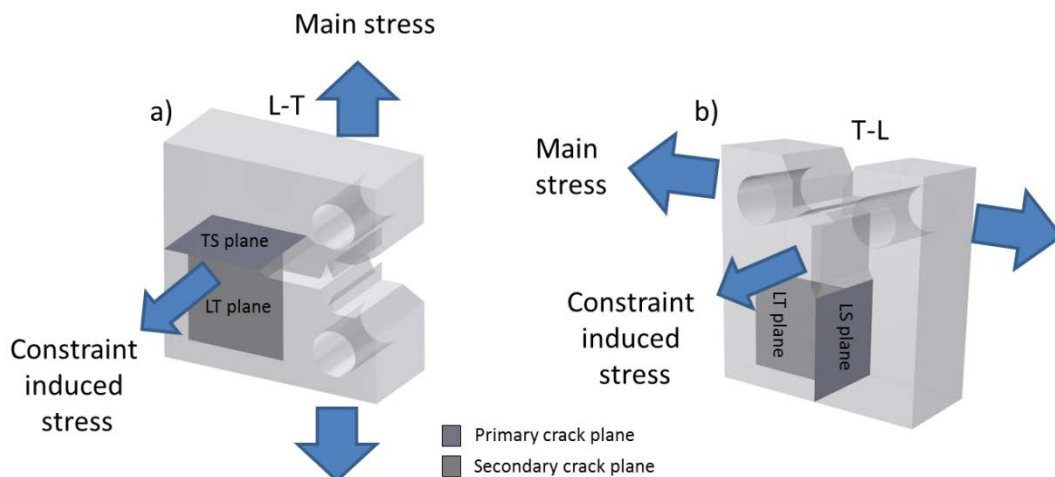


Fig. 5 A schematic illustration of main stress and constraint induced stress in C(T) specimens in (a) L-T orientation and (b) T-L orientation indicating primary and secondary crack planes



Fig. 6 Inverse pole figure Z maps in TS, LT and LS planes

It was found using EBSD grain size distribution analysis, that the grains were ‘pancake’ shaped and had maximum alignment and elongation in L direction followed by T and S directions (Fig. 4). The GAR for fine grains was smaller than coarse grains (Table 2). A detailed statistical grain size analysis in terms of average grain size and GAR is presented in Table 2 and Table 3 for fine and coarse grains respectively. Areas of elongated grains were replaced by circular equivalent areas to calculate the grain sizes. The boundary between fine and coarse grains was chosen by selectively highlighting different size ranges and their coverage over the microstructure. The crystallographic texture map (Fig. 6) shows that the grains were preferentially orientated in $\langle 110 \rangle$ direction parallel to the rolling direction. The fine and the coarse grained regions both had similar texture. It was also observed that $\{100\}$ cleavage planes (depicted by red colour) arranged themselves parallel to the rolling plane (LT plane) (Fig. 6).

Table 2 Grain size analysis for fine grains

Plane	Mean grain size μm	GAR	Number fraction %	Area fraction %
TS (0.3 - 3 μm)	1	2	93.6	20.4
LT (1.4 - 10 μm)	3	1.6	96.1	27.3
LS (0.4 - 3 μm)	1.1	2	93.3	17.6

Table 3 Grain size analysis for coarse grains

Plane	Mean grain size μm	GAR	Number fraction %	Area fraction %
TS (3 - 13 μm)	6	4	6.4	79.6
LT (10 - 91 μm)	21	3.3	4.8	72.7
LS (3 - 16 μm)	6	10	7.4	82.4

3.2 Tensile tests

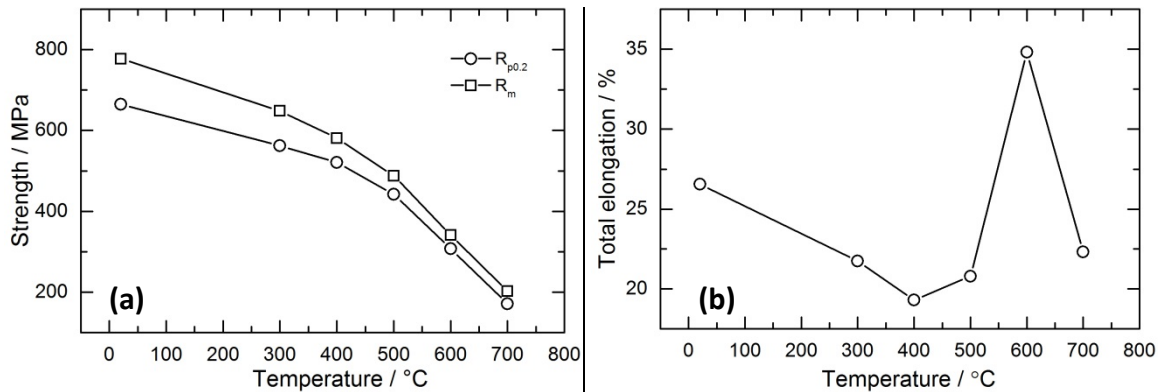


Fig. 7 Yield strength ($R_{p0.2}$) and Ultimate tensile strength (R_m) (a) as well as total elongation (b) variation with temperature for longitudinal miniature tensile tests

The yield strength, the ultimate tensile strength and the total elongation are plotted against temperature are shown in Fig. 7. The material has a yield and ultimate tensile strength of 664 MPa and 777 MPa respectively at RT. The strength decreases with increase in temperature. The total elongation goes down gradually to a minimum value of 19.3% at 400 °C. There is a ductility maximum at 600 °C after which the ductility decreases sharply.

3.3 Fracture toughness tests

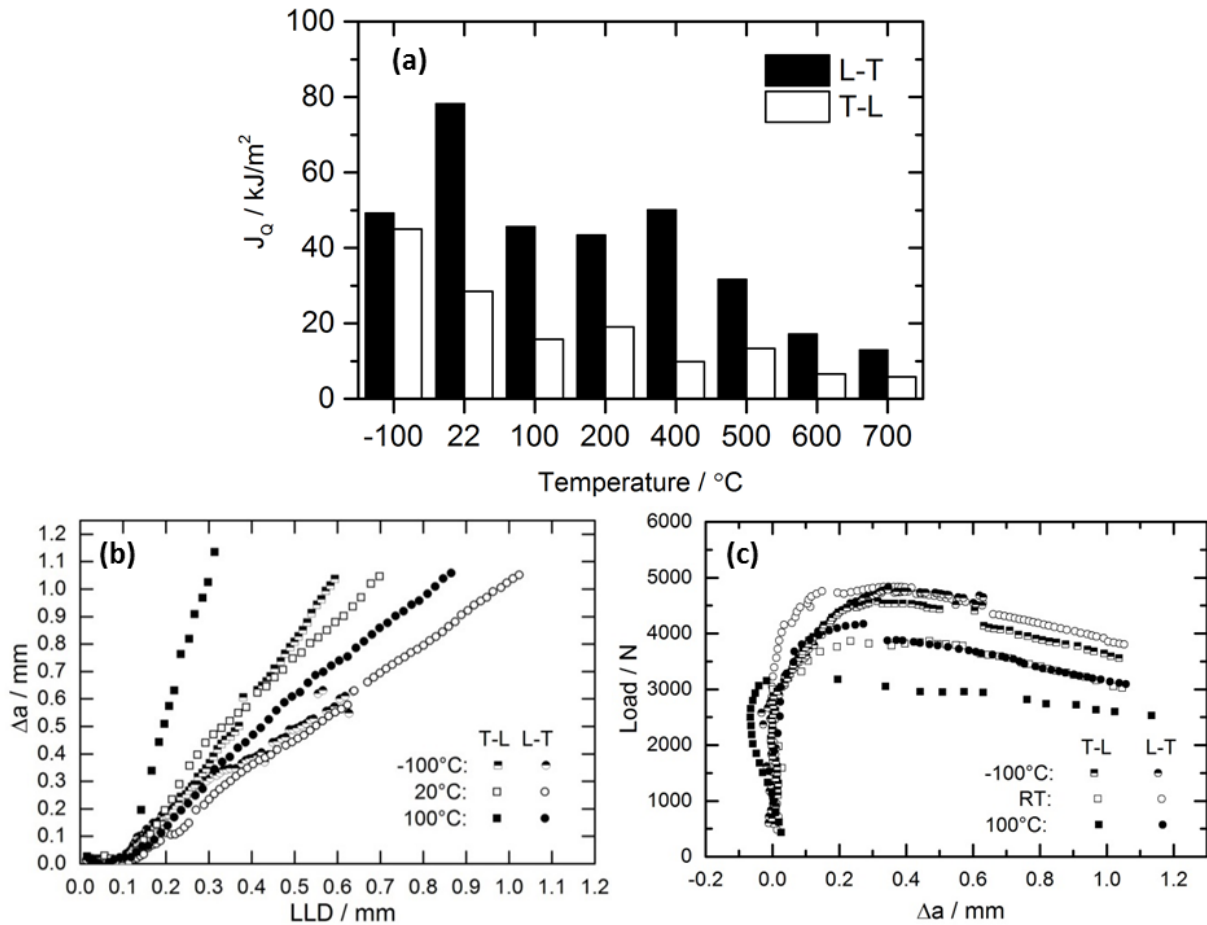


Fig. 8 Comparison of L-T and T-L oriented specimen using (a) J_Q values at various temperatures (b) crack growth versus load line displacement and (c) load versus crack growth

Fig. 8a shows the comparison between L-T and T-L oriented samples tested at various temperatures from $-100\text{ }^\circ\text{C}$ to $700\text{ }^\circ\text{C}$ using J_Q values (provisional J_{IC} values determined by the intersection of the J-R curve with 0.2mm offset line) (Table 4). The energy release rate for elastic-plastic material, J integral, is proportional to the fracture toughness of a material. As expected, a general trend of decreasing fracture toughness (expressed in terms of J_Q) with increasing temperature is observed for both orientations. In L-T orientation, with the exception of RT, the fracture toughness is quite similar up to $400\text{ }^\circ\text{C}$ after which a rapid decrease was observed. T-L orientation exhibited a decrease in fracture toughness with increasing temperatures up to about $400\text{ }^\circ\text{C}$. The fracture toughness of L-T orientation was higher than that of T-L orientation at all temperatures. The T-L oriented samples tested at $200\text{ }^\circ\text{C}$, $400\text{ }^\circ\text{C}$ and $500\text{ }^\circ\text{C}$ encountered unstable crack propagation (suffixed with U in Table 4).

Table 4: Fracture toughness values in both orientations at various temperatures

Temperature °C	J_Q (L-T) kJ/m ²	J_Q (T-L) kJ/m ²
-100	49.2	45
22	78.2	28.4
100	45.6	15.8
200	43.4	19U
400	50.1	9.9U
500	31.6	13.3U
600	17.1	6.5
700	12.9	5.8

3.4 Fracture surfaces

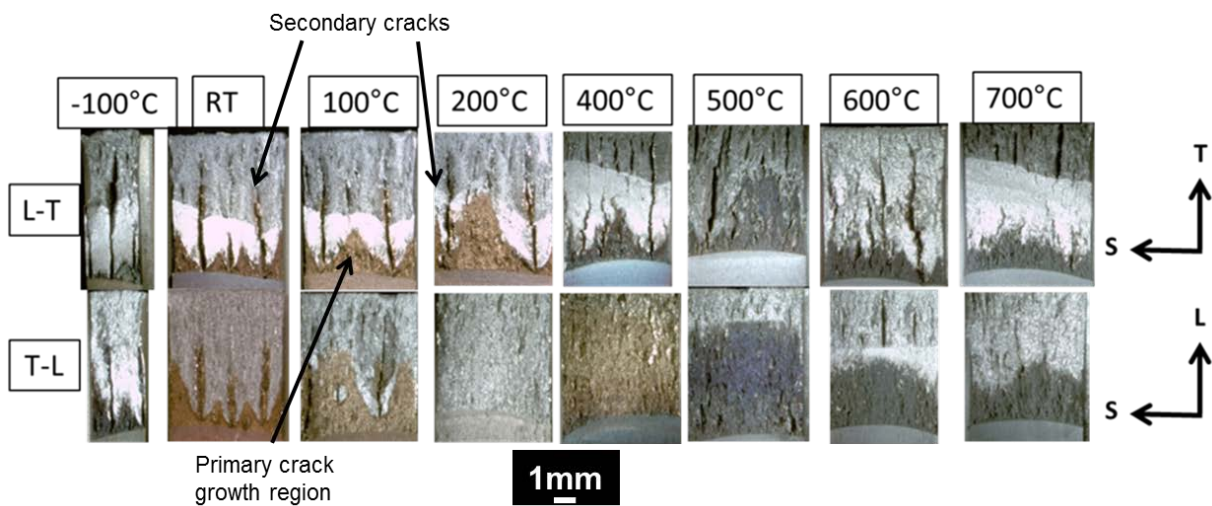


Fig. 9 Stereo microscope images of fractures surfaces at different temperatures and orientations. The primary crack growth region of T-L orientation at 200 °C, 400 °C and 500 °C are not clearly visible due to unstable crack propagation

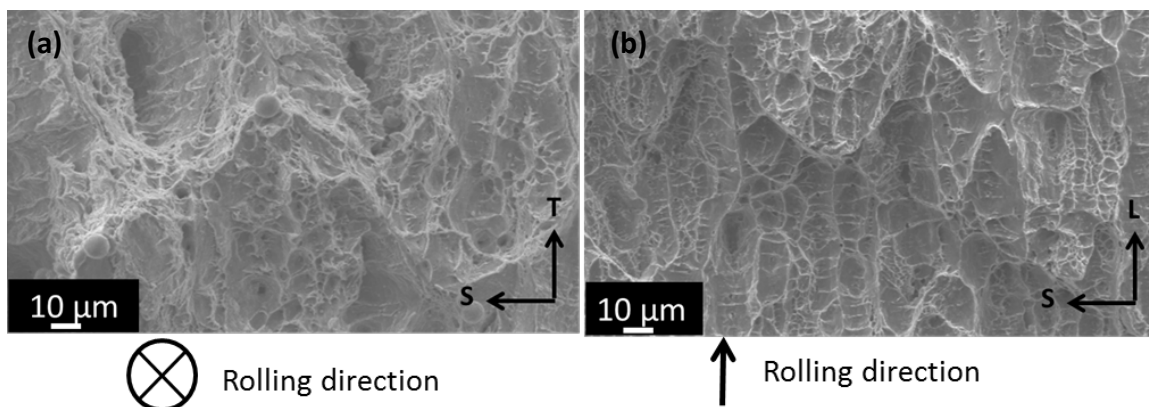


Fig. 10 SEM images of fracture surfaces at RT showing equi-axed dimples in (a) L-T specimen and flat dimples in (b) T-L specimen

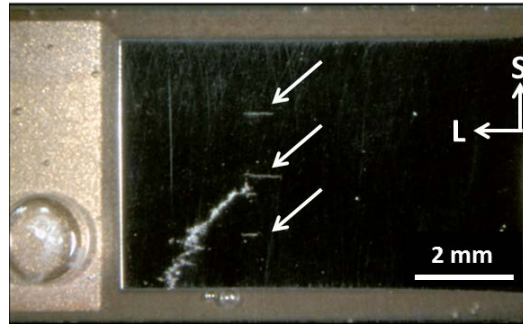


Fig. 11 Interrupted fracture toughness test on T-L specimen. Arrows indicating presence of secondary cracks even before growth of primary crack

Fig. 9 shows the macroscopic stereographic images of the fracture surfaces of L-T and T-L specimen. The green region is the heat tinted non-uniform primary crack growth region. Secondary cracks, growing in a plane perpendicular to primary crack plane and running ahead of the primary crack were observed. Primary crack growth was retarded at regions where secondary cracks grew resulting in its irregular shape. The ASTM nine point method suggests no more than $0.05B$ (where width of C(T) specimen $B = 6.35$ mm) deviation of the individual crack measurements from the average final measured crack length. This condition was not fulfilled due to the irregular nature of the primary crack and hence only a provisional J value (J_Q) could be determined.

Secondary cracks were observed up to 600 °C in L-T oriented specimen. However, they disappeared rather quickly in T-L oriented samples above 100 °C. At 200 °C, 400 °C and 500 °C, T-L oriented specimens experienced load drops in the elastic region during testing (Fig. 9). Secondary cracks were also observed on the primary crack plane in the interrupted fracture toughness test. The secondary cracks initiated even before primary crack growth occurred (Fig. 11).

Fig. 10a and b shows higher magnification pictures of fracture surfaces of L-T and T-L orientation respectively at room temperature. L-T fracture surface was marked with equi-axed dimples whereas flat dimples were observed in T-L orientation.

3.5 EBSD for primary crack propagation

EBSD grain distribution analysis was done on the side surfaces of C(T) specimen (in both orientations) containing the primary crack. The primary crack was perpendicular to the aligned and elongated grains in L-T orientation while it was parallel to them in T-L orientation (Fig. 12a and b). In both L-T and T-L orientation, the primary crack branched out in a direction parallel to rolling direction (L direction) (Fig. 12c - f).

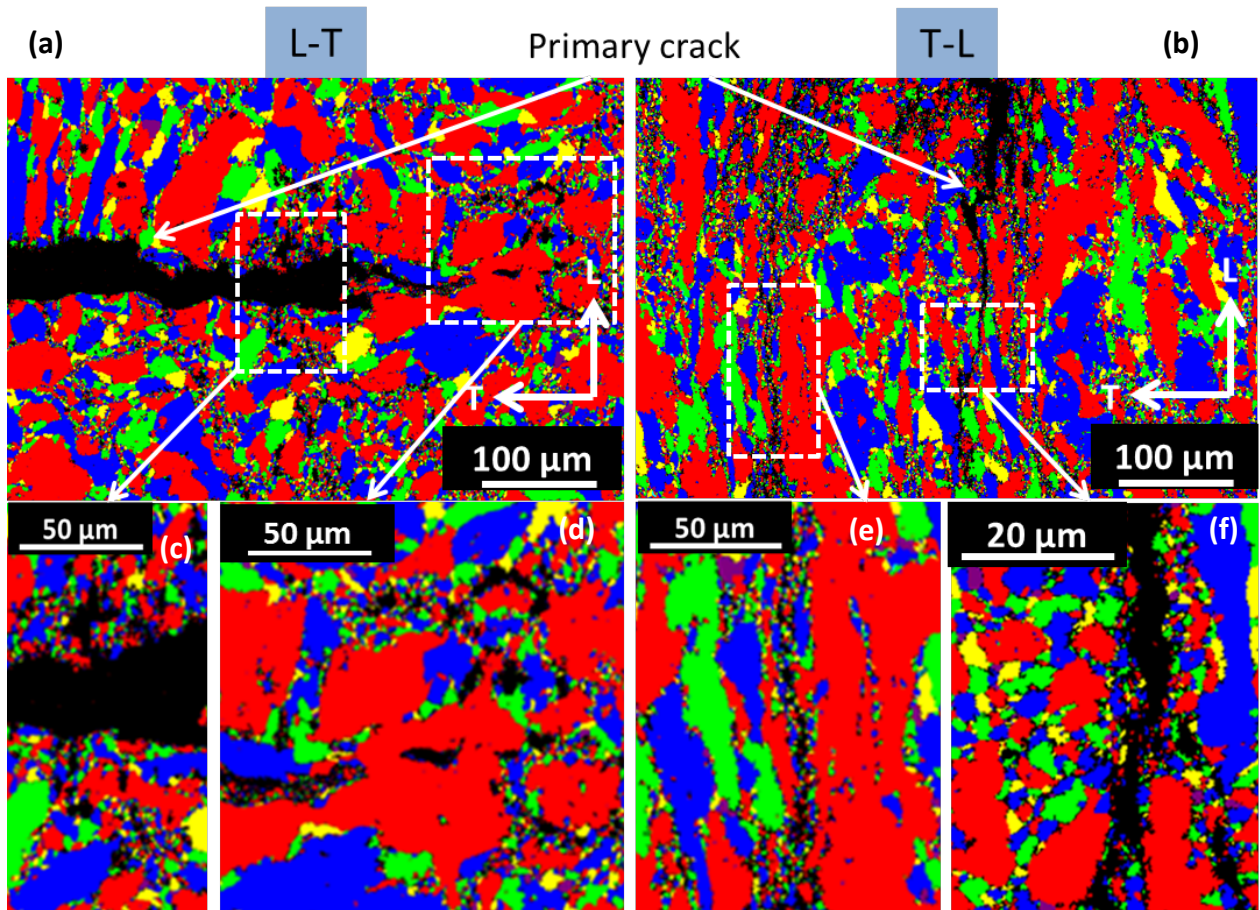


Fig. 12 EBSD grain distribution map of (a) L-T and (b) T-L specimen showing primary crack growth with respect to aligned and elongated grains. Images (c-f) show the magnified regions from images (a) and (b) indicating crack branching

3.6 Secondary crack depths

Secondary crack depths of L-T and T-L specimen tested at 100°C were measured using optical microscope after polishing the LS and TS plane, respectively, at every 0.5 mm secondary crack length. Cumulative crack depths (including all secondary cracks) were measured (Fig. 13). The secondary crack depths were not constant over the length of the secondary crack and reached a maximum at 2.5 mm secondary crack length. It was seen that the number and cumulative depth of secondary cracks in L-T were greater than in T-L orientation. The integral of the curves in Fig. 13c represent one half of the total fracture surface area formed for all secondary cracks.

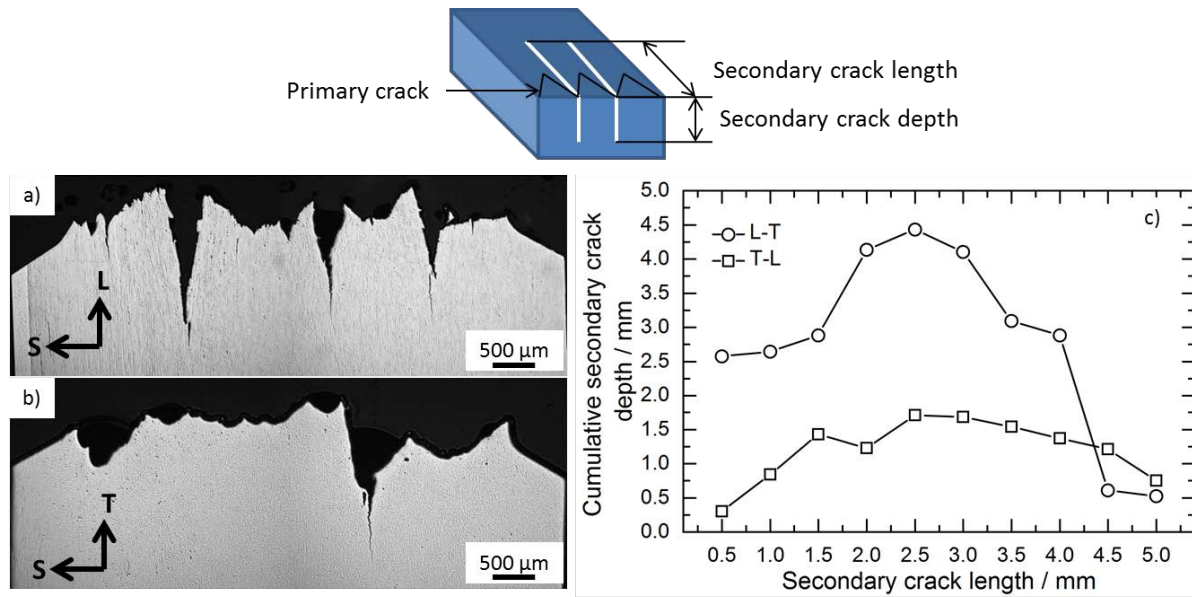


Fig. 13 Optical microscope image showing secondary crack depths after 2.5 mm secondary crack extension at 100 °C in a) L-T and b) T-L specimen. c) Shows the graph between cumulative secondary crack depth and secondary crack length for both orientations

4 Discussion

4.1 Anisotropic primary crack propagation

The fracture toughness of L-T oriented samples was generally found to be higher than that of T-L oriented samples (Fig. 8a) which was in accordance with previous works [6,13]. The dimples found on T-L oriented fracture surface (Fig. 10b) were frequently flat, large and elongated. Similar flat regions were also reported elsewhere [5,15]. This can be expected typically for materials with very low ductility. The L-T oriented fracture surfaces contained equi-axed and deeper dimples, typically expected for ductile materials (Fig. 10a). Low ductility in T-L orientation is supported by Fig. 8b which plots the crack growth versus the load line displacement (LLD) for both orientations at different temperatures during fracture toughness testing. For the same LLD, the crack growth is larger in T-L as compared to L-T specimen at various temperatures due to lower ductility.

In the brittle regime ($-100\text{ }^{\circ}\text{C}$), both the primary crack propagation planes in L-T and T-L oriented specimens (TS and LS planes respectively) were perpendicular to the $\{100\}$ cleavage planes which were aligned parallel to the rolling plane (LT plane) (Fig. 6). Therefore they didn't get any assistance towards primary crack propagation. In the ductile regime ($> \text{RT}$) however, crack propagation occurred through void growth and coalescence (Fig. 10). It was found in [28] using simulation of a bcc single crystal that void growth and coalescence was easiest in $\langle 110 \rangle$ direction. As most grains had a $\langle 110 \rangle$ texture towards rolling direction (L direction) (Fig. 6), primary crack propagation in the ductile regime was easiest in this direction.

The aligned Ti enriched particles (Fig. 3) also contributed to anisotropic fracture behaviour. Trans-granular dimple formation, which was quite often observed on fracture surfaces (Fig. 10), were a result of void growth and coalescence originating from these Ti enriched particles. The alignment of these particles parallel to rolling direction meant easier crack propagation via dimple formation along rolling direction. Thus T-L oriented samples (primary crack propagation towards L direction) had lower fracture toughness than L-T oriented samples. The ODS steel had bimodal microstructure which was elongated due to hot rolling (Fig. 4).

Many of the fine grains, especially less than 1 μm could be classified as ultra-fine grains (UFGs) [29]. The mechanical properties of UFGs are different from that of coarse grains with respect to strength and deformation capability. Coarse grains have lesser strength and are able to deform much more than fine grains as dislocations can interact with each other within the grains forming dislocation cells. UFGs have a lower deformation capability as dislocations assemble and rearrange themselves at grain boundary reaching saturation [10,29–31]. This is associated with hardening leading to a higher yield stress with evolving plastic strain. The crack propagation in the C(T) specimens preferentially followed the fine grained region (Fig. 12). During loading of C(T) specimen, the coarse grains reached their yield point first and deformed plastically. The fine grains reached their yield point next, but could not plastically deform much, thus initiating voids which assisted the primary crack to propagate. Similar fracture behaviour for a non ODS bimodal alloy was seen in [30].

The primary crack propagation in T-L specimen (in L direction) had a relatively free path (Fig. 12b) through the fine grains (aligned in L direction) and did not face obstruction from the coarse grains which were elongated parallel to the rolling direction (L direction) and had a GAR value of 10 in the LS plane. The primary crack propagation in L-T specimen (in T direction) was less assisted by fine grains (aligned parallel to rolling direction) and coarse grains which had a GAR value of 4 in the TS plane. The primary crack in L-T specimen was actually blunted by the coarse grains, which were elongated more towards L direction than towards the T direction (Fig. 12a). Similar mechanism was also seen in [30]. Crack branching in the fine grains was observed to be aligned in a direction parallel to the rolling direction in both L-T (Fig. 12c and d) and T-L orientations (Fig. 12e and f). The dissipation of energy by crack branching is more in L-T than in T-L orientation as the crack has to deviate more from its original path (along primary crack). This energy dissipation by branching inhibits the primary crack propagation. The energy required to propagate primary crack in L-T oriented specimen was therefore more than in T-L oriented specimen resulting in higher fracture toughness.

4.2 Anisotropic secondary crack propagation

Secondary cracks were seen on the fracture surfaces of both orientations as they had the same plane (LT plane in Fig. 5). Secondary cracking was also reported in other studies [9,11,15,16]. They seem to be a common feature of certain sample orientations, such as L-T and T-L investigated here, classified as crack divider geometries [32]. Crack divider geometries have a specific crack propagation direction with respect to the anisotropic microstructure, which results in secondary cracks dividing the specimen thickness into sub-specimens [8]. Contrary to the primary crack, no fatigue pre-crack was available for the initiation of secondary cracks. Therefore, the initiation of secondary cracks must have occurred through micro-cracks or through de-cohesion of Ti enriched particles with the matrix, lying on the primary crack plane.

In this context, it is interesting to note that the secondary cracks initiated earlier than the primary cracks at lower loads. They appeared early during testing, even before primary crack growth (at a low J value of 14 kJ/m^2) as seen from Fig. 11. This early initiation was due to the ease of crack propagation in secondary crack plane (LT) than in primary crack plane (TS plane for L-T and LS plane for T-L) (Fig. 5). In the rolling direction (L), as mention in section 4.1, preferential alignment of elongated fine and coarse grains along with Ti enriched particles were observed. Hence it was easier for the crack to propagate along L direction followed by T and S directions. The LT plane contained both L and T directions as compared to only one elongated direction L or T in LS or TS plane, respectively.

It was also found that {100} cleavage planes facilitated secondary cracking in certain orientations [33]. In the brittle regime, in both L-T and T-L orientations, the secondary crack plane was the same (LT plane) which contained the {100} cleavage planes aligned parallel to rolling plane (Fig. 6). Therefore both orientations had equal assistance from {100} cleavage planes towards secondary crack formation. In the ductile regime, void growth and coalescence was easier towards $\langle 110 \rangle$ direction (L direction) as compared to T direction [28].

The secondary crack propagated both perpendicular and parallel to the primary crack direction (LT plane in Fig. 5). The primary crack growth was retarded near the secondary cracks due to the reduction of the local driving forces which originated due to a shift to plane stress condition from a plane strain condition. This increased the overall fracture toughness which was similar to the results obtained experimentally as well as by 3D finite element computations in another work [34]. It was evident from the fracture surfaces that the secondary cracks showed a tendency to get arrested and become shallower with increasing temperature due to crack tip blunting (Fig. 9). Their contribution to energy absorption and fracture toughness enhancement was therefore lesser at higher temperature.

The existence of secondary cracks not only increased the amount of energy absorbed during fracture, but also helped in stabilization of primary crack propagation. The ease of primary crack propagation in T-L oriented specimen (section 4.1) generally tended to make primary crack propagation unstable in these specimens. However, from $-100\text{ }^{\circ}\text{C}$ up to $100\text{ }^{\circ}\text{C}$, T-L oriented specimen showed stable primary crack propagation due to existence of secondary cracks which increased energy absorption (Fig. 9). Similar energy absorption was observed in crack divider geometry at low temperatures due to secondary cracking in [33]. The secondary cracks absorbed energy and lowered the local driving force for growth of primary crack in its vicinity, thus making it propagate in a stable manner. The secondary cracks became shallower and disappeared near $200\text{ }^{\circ}\text{C}$ in T-L samples due to secondary crack tip blunting. The primary crack propagation therefore became unstable at $200\text{ }^{\circ}\text{C}$ as primary crack propagated freely (Fig. 9). Increasing the temperature up to $500\text{ }^{\circ}\text{C}$ reduced the amount of secondary cracks further and led to an increase in plasticity at primary crack tip. This increase in primary crack tip plasticity counter balanced the crack instability created by free primary crack propagation in the earlier stage. Therefore, the primary crack stabilized again at higher temperatures. Despite these effects of secondary cracks, more investigations are needed with respect to component fracture testing as secondary cracks initiated earlier than the primary crack at lower loads (Fig. 11).

More pronounced secondary crack propagation was observed in L-T oriented specimens than in T-L oriented specimens (Fig. 9). Secondary cracking occurs due to constrained induced stress which directly depends on the main stress. If the main stresses were equal in L-T and T-L orientations, the secondary cracks in both L-T and T-L orientations would have had the same cumulative energy dissipation (as they lie on the same LT plane). However, the main stress was lower in T-L than in L-T oriented specimen for the same primary crack propagation at most temperatures (Fig. 8c). This was due to easier primary crack propagation in T-L orientation (section 4.1). Hence the constraint induced stress was also less in T-L oriented specimen resulting in lesser assistance for secondary crack propagation (Fig. 13). This also explains the early disappearance of secondary cracks with increasing temperature in T-L oriented specimens.

5 Conclusions

- Primary cracks propagated preferentially through the fine grained region. The fine grained regions consisted of UFGs which are known to have lower ductility than coarse grains. UFGs initiated voids after reaching their yield stress during loading.
- Crack propagation was easiest along rolling direction (L), as the fine and the coarse grains were most aligned and elongated in this direction (highest GAR). Crack propagation preference was lower in T and in S directions. Therefore primary crack propagation in T-L oriented specimen was easier than L-T oriented specimen resulting in lower fracture toughness.
- Preferential alignment of Ti rich particles along the rolling direction and easier void growth and coalescence in <110> direction helped in trans-granular dimple formation and contributed to easier fracture along rolling direction. This contributed to lower fracture toughness in T-L specimens.
- Secondary cracks absorbed energy and locally lowered the driving force for primary crack growth. In T-L specimen, secondary crack stabilized primary crack propagation at lower temperatures. Secondary cracks initiated at lower loads as compared to primary cracks. This was due to the relative ease of secondary crack propagation along aligned and elongated grains in LT plane as compared to primary crack propagation in TS and LS planes in L-T and T-L orientations, respectively. Crystallographic texture also contributed towards secondary crack anisotropy.
- Secondary crack propagation was more pronounced in terms of the frequency of their occurrence and depth in L-T orientation than in T-L orientation due to higher constraint induced stress available for its growth.

Acknowledgements

The authors would like to thank Mr. Wolfgang Webersinke and Mr. Mario Houska for their contributions to the fracture mechanics testing of C(T) specimens, Ms. Gudrun Müller for her contributions to EBSD & SEM investigations and Ms. Michaela Rossner for metallographic preparations. Additional thanks to our colleagues at the workshop.

This work contributes to the Joint Programme on Nuclear Materials (JPNM) of the European Energy Research Alliance (EERA).

References

- [1] P. Dubuisson, Y. de Carlan, V. Garat, M. Blat, ODS Ferritic/martensitic alloys for Sodium Fast Reactor fuel pin cladding, *J. Nucl. Mater.* 428 (2012) 6–12. doi:10.1016/j.jnucmat.2011.10.037.
- [2] R.L. Klueh, P.J. Maziasz, I.S. Kim, L. Heatherly, D.T. Hoelzer, N. Hashimoto, E.A. Kenik, K. Miyahara, Tensile and creep properties of an oxide dispersion-strengthened ferritic steel, *J. Nucl. Mater.* 307–311, Part 1 (2002) 773–777. doi:10.1016/S0022-3115(02)01046-2.
- [3] M.K. Miller, D.T. Hoelzer, E.A. Kenik, K.F. Russell, Stability of ferritic MA/ODS alloys at high temperatures, *Intermetallics*. 13 (2005) 387–392. doi:10.1016/j.intermet.2004.07.036.
- [4] A. KIMURA, H.-S. CHO, N. TODA, R. KASADA, K. YUTANI, H. KISHIMOTO, N. IWATA, S. UKAI, M. FUJIWARA, High Burnup Fuel Cladding Materials R&D for Advanced Nuclear

- Systems, *J. Nucl. Sci. Technol.* 44 (2007) 323–328.
doi:10.1080/18811248.2007.9711289.
- [5] T.S. Byun, J.H. Kim, J.H. Yoon, D.T. Hoelzer, High temperature fracture characteristics of a nanostructured ferritic alloy (NFA), *J. Nucl. Mater.* 407 (2010) 78–82.
doi:10.1016/j.jnucmat.2010.09.031.
- [6] H. Hadraba, B. Fournier, L. Stratil, J. Malaplate, A.-L. Rouffié, P. Wident, L. Ziolek, J.-L. Béchade, Influence of microstructure on impact properties of 9–18%Cr ODS steels for fusion/fission applications, *J. Nucl. Mater.* 411 (2011) 112–118.
doi:10.1016/j.jnucmat.2011.01.038.
- [7] M. Serrano, M. Hernández-Mayoral, A. García-Junceda, Microstructural anisotropy effect on the mechanical properties of a 14Cr ODS steel, *J. Nucl. Mater.* 428 (2012) 103–109. doi:10.1016/j.jnucmat.2011.08.016.
- [8] J. Chao, C. Capdevila, M. Serrano, A. Garcia-Junceda, J.A. Jimenez, G. Pimentel, E. Urones-Garrote, Notch Impact Behavior of Oxide-Dispersion-Strengthened (ODS) Fe20Cr5Al Alloy, *Metall. Mater. Trans. A.* 44 (2013) 4581–4594. doi:10.1007/s11661-013-1815-7.
- [9] J.H. Kim, T.S. Byun, D.T. Hoelzer, Tensile fracture characteristics of nanostructured ferritic alloy 14YWT, *J. Nucl. Mater.* 407 (2010) 143–150.
doi:10.1016/j.jnucmat.2010.09.054.
- [10] A. Chauhan, D. Litvinov, J. Aktaa, High temperature tensile properties and fracture characteristics of bimodal 12Cr-ODS steel, *J. Nucl. Mater.* 468 (2016) 1–8.
doi:10.1016/j.jnucmat.2015.11.013.
- [11] M. Serrano, A. García-Junceda, R. Hernández, M.H. Mayoral, On anisotropy of ferritic ODS alloys, *Mater. Sci. Technol.* 30 (2014) 1664–1668.
doi:10.1179/1743284714Y.0000000552.
- [12] A. García-Junceda, M. Hernández-Mayoral, M. Serrano, Influence of the microstructure on the tensile and impact properties of a 14Cr ODS steel bar, *Mater. Sci. Eng. A.* 556 (2012) 696–703. doi:10.1016/j.msea.2012.07.051.
- [13] A.L. Rouffié, P. Wident, L. Ziolek, F. Delabrouille, B. Tanguy, J. Crépin, A. Pineau, V. Garat, B. Fournier, Influences of process parameters and microstructure on the fracture mechanisms of ODS steels, *J. Nucl. Mater.* 433 (2013) 108–115.
doi:10.1016/j.jnucmat.2012.08.050.
- [14] T.S. Byun, J.H. Yoon, S.H. Wee, D.T. Hoelzer, S.A. Maloy, Fracture behavior of 9Cr nanostructured ferritic alloy with improved fracture toughness, *J. Nucl. Mater.* 449 (2014) 39–48. doi:10.1016/j.jnucmat.2014.03.007.
- [15] R. Kasada, S.G. Lee, J. Isselin, J.H. Lee, T. Omura, A. Kimura, T. Okuda, M. Inoue, S. Ukai, S. Ohnuki, T. Fujisawa, F. Abe, Anisotropy in tensile and ductile–brittle transition behavior of ODS ferritic steels, *J. Nucl. Mater.* 417 (2011) 180–184.
doi:10.1016/j.jnucmat.2010.12.069.
- [16] M.J. Alinger, G.R. Odette, G.E. Lucas, Tensile and fracture toughness properties of MA957: implications to the development of nanocomposited ferritic alloys, *J. Nucl. Mater.* 307–311, Part 1 (2002) 484–489. doi:10.1016/S0022-3115(02)01220-5.

- [17] E. Altstadt, M. Serrano, M. Houska, A. García-Junceda, Effect of anisotropic microstructure of a 12Cr-ODS steel on the fracture behaviour in the small punch test, *Mater. Sci. Eng. A.* 654 (2016) 309–316. doi:10.1016/j.msea.2015.12.055.
- [18] B.L. Bramfitt, A.R. Marder, A study of the delamination behavior of a very low-carbon steel, *Metall. Trans. A.* 8 (1977) 1263–1273. doi:10.1007/BF02643841.
- [19] D.L. Bourell, O.D. Sherby, Texture induced cleavage delamination of warm-rolled low carbon steel, *Metall. Trans. A.* 14 (1983) 2563–2566. doi:10.1007/BF02668900.
- [20] J.H. Kim, T.S. Byun, D.T. Hoelzer, S.-W. Kim, B.H. Lee, Temperature dependence of strengthening mechanisms in the nanostructured ferritic alloy 14YWT: Part I—Mechanical and microstructural observations, *Mater. Sci. Eng. A.* 559 (2013) 101–110. doi:10.1016/j.msea.2012.08.042.
- [21] A. Chauhan, D. Litvinov, Y. de Carlan, J. Aktaa, Study of the deformation and damage mechanisms of a 9Cr-ODS steel: Microstructure evolution and fracture characteristics, *Mater. Sci. Eng. A.* 658 (2016) 123–134. doi:10.1016/j.msea.2016.01.109.
- [22] B. Shashank Dutt, M. Nani Babu, S. Venugopal, G. Sasikala, A.K. Bhaduri, Effect of test temperature on fracture toughness of modified 9Cr–1Mo steel, *Mater. Sci. Technol.* 27 (2011) 1527–1533. doi:10.1179/026708310X12815992418094.
- [23] F. Ersoy, S. Gavrilov, K. Verbeken, Investigating liquid-metal embrittlement of T91 steel by fracture toughness tests, *J. Nucl. Mater.* 472 (2016) 171–177. doi:10.1016/j.jnucmat.2015.12.019.
- [24] J. Hoffmann, M. Rieth, L. Commin, S. Antusch, Microstructural anisotropy of ferritic ODS alloys after different production routes, *Fusion Eng. Des.* 98–99 (2015) 1986–1990. doi:10.1016/j.fusengdes.2015.05.002.
- [25] K. Arora, H. Viehrig, Evaluation of the ASTM and ISO J Initiation Procedures by Applying the Unloading Compliance Technique to Reactor Pressure Vessel Steels, *Eval. ASTM ISO J Initiat. Proced. Appl. Unloading Compliance Tech. React. Press. Vessel Steels.* (2011).
- [26] ASTM Standard E1820-13, Standard test method for measurement of Fracture Toughness, (n.d.).
- [27] Kim Wallin, *Fracture Toughness of Engineering Materials - Estimation and application*, EMAS Publishing, 2011.
- [28] S.K. Yerra, C. Tekog˘lu, F. Scheyvaerts, L. Delannay, P. Van Houtte, T. Pardoen, Void growth and coalescence in single crystals, *Int. J. Solids Struct.* 47 (2010) 1016–1029. doi:10.1016/j.ijsolstr.2009.12.019.
- [29] H. Liu, Y. Shen, J. Ma, P. Zheng, L. Zhang, Grain Size Dependence of Uniform Elongation in Single-Phase FCC/BCC Metals, *J. Mater. Eng. Perform.* 25 (2016) 3599–3605. doi:10.1007/s11665-016-2245-7.
- [30] Z. Lee, V. Radmilovic, B. Ahn, E.J. Lavernia, S.R. Nutt, Tensile Deformation and Fracture Mechanism of Bulk Bimodal Ultrafine-Grained Al-Mg Alloy, *Metall. Mater. Trans. A.* 41 (2009) 795–801. doi:10.1007/s11661-009-0007-y.
- [31] M.S. Oskooie, H. Asgharzadeh, Strength and ductility enhancement in nanostructured Al6063 with a bimodal grain size distribution, *IOP Conf. Ser. Mater. Sci. Eng.* 63 (2014) 012022. doi:10.1088/1757-899X/63/1/012022.

- [32] Y. Kimura, T. Inoue, F. Yin, K. Tsuzaki, Delamination Toughening of Ultrafine Grain Structure Steels Processed through Tempforming at Elevated Temperatures, *ISIJ Int.* 50 (2010) 152–161. doi:10.2355/isijinternational.50.152.
- [33] S. Ukai, W. Izawa, N. Oono, S. Hayashi, Y. Kohno, S. Ohtsuka, T. Kaito, Charpy impact property related to 100 cleavage fracture in 15CrODS steel, *Mater. Sci. Technol.* 30 (2014) 1709–1714. doi:10.1179/1743284714Y.0000000604.
- [34] S. Kalyanam, A.J. Beaudoin, R.H. Dodds Jr., F. Barlat, Delamination cracking in advanced aluminum–lithium alloys – Experimental and computational studies, *Eng. Fract. Mech.* 76 (2009) 2174–2191. doi:10.1016/j.engfracmech.2009.06.010.